ADVANCED ENERGY MATERIALS

Supporting Information

for *Adv. Energy Mater.,* DOI: 10.1002/aenm.201301937

Broadband Plasmonic Photocurrent Enhancement in Planar Organic Photovoltaics Embedded in a Metallic Nanocavity

*Matthew E. Sykes, Adam Barito, Jojo A. Amonoo, Peter F. Green, and Max Shtein**

Submitted to ADVANCED ENERGY MATERIALS

Supporting Information

for *Adv. Energy Mater.*, DOI: 10.1002/aenm.201301937

Broadband Plasmonic Photocurrent Enhancement in Planar Organic Photovoltaics Embedded in a Metallic Nanocavity

*Matthew E. Sykes, Adam Barito, Jojo A. Amonoo, Peter F. Green, and Max Shtein**

1. ATR Spectroscopy

A detailed schematic diagram of the custom-built attenuated total reflection (ATR) Kretschmann setup for testing the dispersion of both EQE and reflectivity of OPV devices is shown in **Figure S1**. Light from a halogen lamp was coupled into a monochromator (Newport 130 1/8m), with its output calibrated to a spectral full width at half maximum (FWHM) of 5 nm. A series of lenses and an aperture were used to collimate the beam divergence to less than 1° and remove spherical aberrations. A calcite glan-thompson polarizer was then used to polarize the light to either TM- or TE-polarization. Light was directed to either a calibrated silicon reference cell or the sample, following an identical optical path length in each case. To maximize photocurrent signal, we employed the overfilling method of device illumination, whereby the beam size exceeds the device area. Since devices used in this study had a diameter of 1 mm, a 1 mm diameter circular aperture was used on the reference cell and positioned to capture the same portion of the incident beam.

The use of the overfilling method during ATR-based EQE testing requires we correct for focusing effects from the hemicylindrical prism, as the average beam intensity over the projected device area varies with angle. We are able to extract the focusing factor as a function of angle by comparing the normalized angular response of the EQE under TE-polarized illumination to that predicted by our model (**Figure S2**). As can be seen here, after accounting for the angular intensity variation, we show an excellent agreement between the TM-polarized

response, reproducing the SPR peak to within 1° offset. This small shift is likely due to the effect of surface roughness at the Ag/air interface, as the location of the dip in EQE at the on-set of total internal reflection from the glass/Ag interface matches exactly. This normalization was performed for each individual device tested to ensure minor device-to-device variations in electrode size from shadow masking did not impact the focusing factor, and is accounted for in all of the ATR-based EQE data shown in this study.

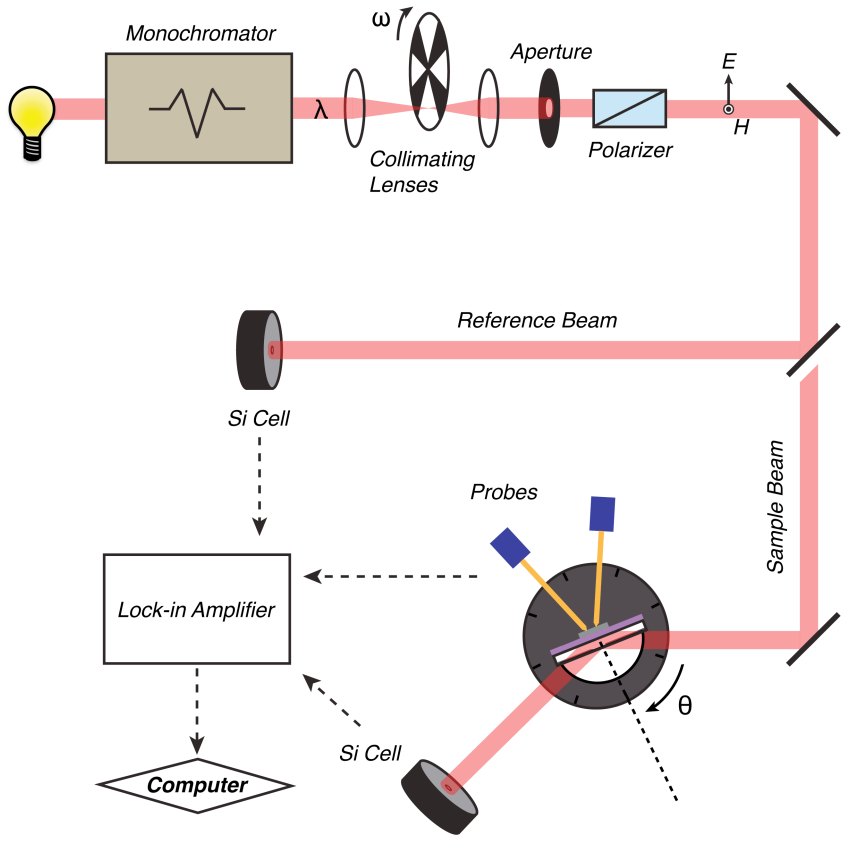

Figure S1. Schematic diagram of the Kretschmann configuration based ATR setup used in this study for probing the spectral and angular response of the device EQE and reflectivity.

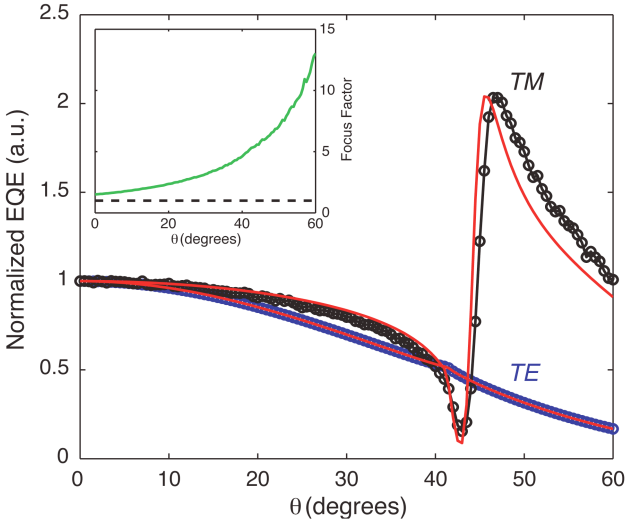

Figure S2. Example fitting of normalized EQE versus incident angle of an inverted device for TE and TM-polarized light. After accounting for the focusing factor (*Inset*) we observe excellent agreement between experiment and prediction for the SPR response. The focusing factor at normal incidence was calculated experimentally by scanning the EQE of the device with and without the prism, and accounts for the additional incoupling compared to the bare aperture of the reference cell.

In the case of angular reflectivity measurements using ATR (Figures 4b and 4b), unmasked films deposited simultaneously with the inverted and conventional devices (**Figures S3c** and **S3f**, respectively) were used so the entirety of the reflected light could be collected. To ensure the same portion of the beam was being probed as the devices in Figures 4d and 4d, an additional 1mm diameter aperture was inserted directly before the prism. Finally a calibrated silicon reference cell was attached to the motorized stage to capture the reflected light. This data was compared to a 150 nm thick Ag mirror as a 100 %R reference over the same angle-wavelength range. Because the projected area of the device stacks and silver mirrors remained unchanged during measurement (samples were effectively underfilled), there was no need to use a normalization to account for focusing from the prism.

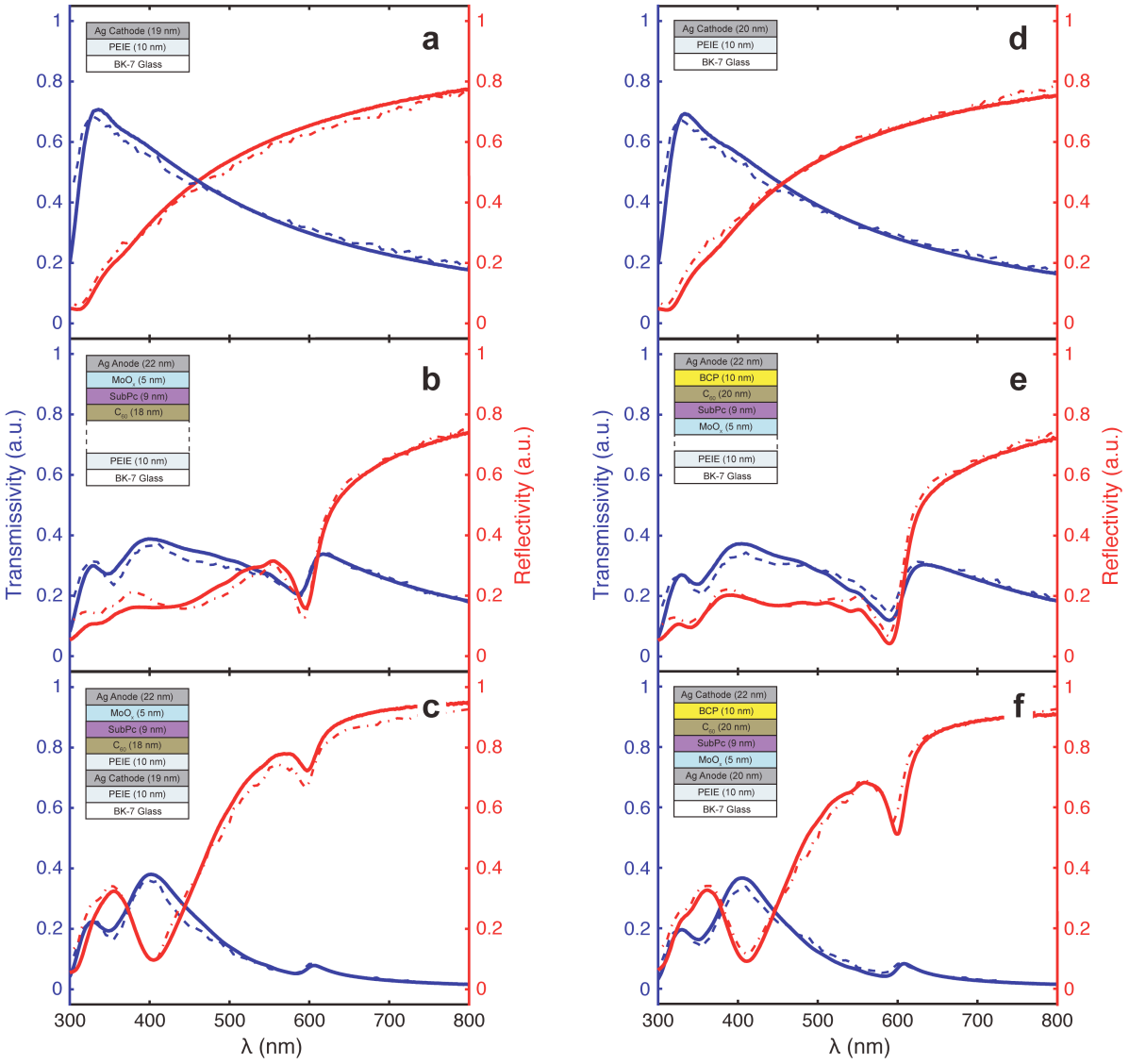

Figure S3. Reflectivity (red lines) and transmissivity (blue lines) spectra taken for sequentially deposited layers of both devices, measured at 7.5° and normal incidence respectively. Plots include **(a,d)** the silver cathode/anode, **(b,e)** organic layers and anode/cathode, and **(c,f)** complete inverted/conventional device structure. Modeled reflectivity (dash) and transmissivity (dot dash) spectra are included, showing the accuracy of the optical transfer-matrix model used in this study. Insets show the sample structures corresponding to each set of spectra, with dotted lines indicating the omitted layers.

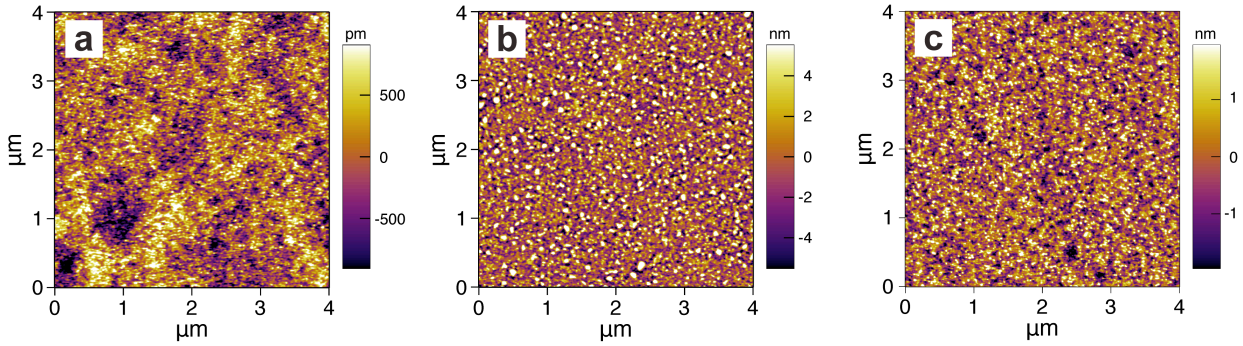

Figure S4. Tapping mode AFM micrographs of the surfaces of **(a)** the bottom Ag electrode, **(b)** top Ag electrode (anode) for the inverted devices, and **(c)** top Ag electrode (cathode) for the conventional geometry. The corresponding device structures are shown in Figures S3a, S3c, and S3f, respectively. Up to an order of magnitude higher roughness is observed for the two top electrodes, which we attribute to the underlying organic active layers.

2. AFM Roughness Measurements

Atomic force microscopy (AFM) was carried out on the electrodes of both device structures, as can be seen in **Figure S4**. Since the bottom electrode structure Glass/PEIE/Ag was unchanged between both inverted and conventional devices, Figure S4a is representative of both device structures. Because Ag is known to island on glass without a wetting layer, we employed PEIE as a semitransparent adhesion layer for the bottom electrode. This application of PEIE is uniquely suited for ATR spectroscopy techniques as it has a refractive index matched to glass and is completely non-absorbing in the visible spectrum, unlike metallic adhesion layers such as Ti. This allows the growth of pure, ultra-smooth Ag films without changing the local dielectric environment or plasmonic response of the metal. Indeed there is no presence of localized SPR in the transmission/reflection spectra (Figures S3a and S3c) indicative of Ag islanding, which we observed to be completely stable at room temperature.

In comparison, the top electrodes in both device structures exhibited up to an order of magnitude larger roughness due to the inherent roughness of the underlying organic layers. While the quality of the Ag/air interface is critical to the damping of the SPP_1 mode propagation, our early experiments indicated the bottom electrode plays a pivotal role in the predicta-

bility of the angular EQE and reflectivity response. As it is the most easily adjusted, every effort should be made to eliminate the lower electrode's roughness. This allows for accurate device modeling to be performed using literature values of refractive indices, without the need for effective refractive index fitting of constituent layers.

3. ATR Spectroscopy of a Conventional Device

As can be seen in **Figure S5**, both the reflectivity and EQE are accurately matched between model and experiment for the conventional device. Again, we observe a slight

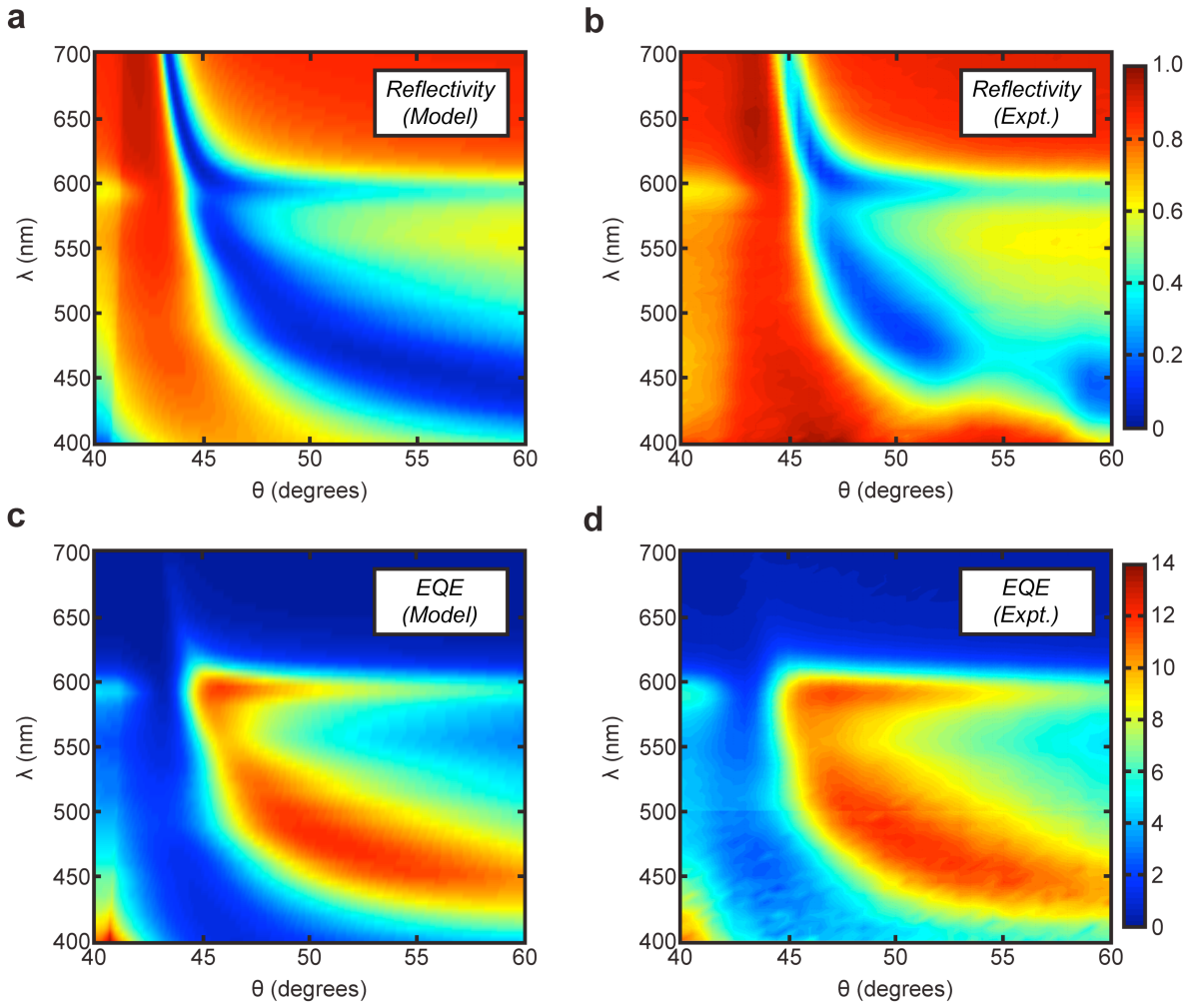

Figure S5. (a) Modeled and **(b)** measured reflectivity (a.u.) as a function of the incidence angle (in glass) and free-space wavelength for the conventional MDM device structure. The corresponding device EQE (%) as a function of angle and wavelength is also shown for both **(c)** modeled and **(d)** measured values. Note the same scale bars are used for both model and experiment.

discrepancy between measured and modeled reflectivity at the C_{60} aborption peak (λ = 460 nm), consistent with the inverted geometry. This asymmetry in the CT-exciton absorption does not appear to affect the observed performance, as the increased reflectivity is directly offset by an increase in absorption within the C_{60} active layer. Finally, we note the presence of some horizontal and vertical linear artifacts in Fig. 4d and Fig. S5d, which are due to the interpolation of the colormap used in the figures and should not be considered physically relevant. The horizontal artifact at λ = 500 nm is due to a switch in the lock-in amplifier sensitivity, as the measurement scans were broken up into two separate wavelength ranges to maximize the signal-to-noise ratio.

4. EQE Enhancement Factor

As mentioned in the main text (Section 2.5), the measured EQE enhancement factor peaks at 4.3x for the inverted device geometry. Considering the IQE for this device is relatively flat across the visible spectrum, and η_{CC} is consistent between normal incidence and SPR, our simulations predict a higher EQE enhancement factor at longer wavelengths approaching 700 nm. Indeed the simulated absorption enhancement reaches 9x for this structure at 700 nm.

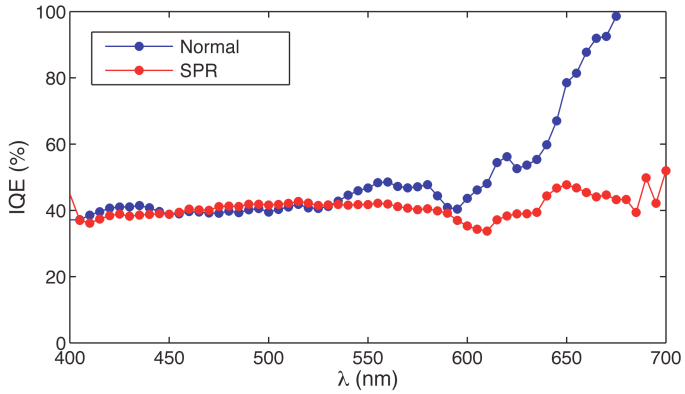

Figure S6. Measured IQE values for the inverted device at normal incidence (blue circles) and SPR (red circles). The higher absorption at long wavelengths at SPR yields a high signal-to-noise ratio, producing a flat IQE across the visible spectrum. At normal incidence, minimal photocurrent generation past 625 nm gives a low signal-to-noise ratio and an unphysically large IQE. For this reason, the measured EQE enhancement is reduced below predicted values.

The reason for the sharp decline in EQE enhancement past ~625 nm can be entirely attributed to a low signal-to-noise ratio during EQE testing at normal incidence. This yields an unphysically large IQE past 625 nm for the inverted device at normal incidence (**Figure S6**). Since the EQE enhancement factor is the ratio of EQE at SPR to EQE at normal incidence, it is thus lower than that predicted by simulation.